Nanoscale Advances

ROYAL SOCIETY OF CHEMISTRY

PAPER

View Article Online
View Journal | View Issue

Check for updates

Cite this: *Nanoscale Adv.*, 2025, **7**, 1118

CeO_x-anchored β-$Ni(OH)_2$ nanosheets onto nickel foam for efficient energy-saving hydrogen production *via* an electrocatalytic glucose oxidation reaction†

Cong Hong Nhat Nguyen,‡[a] Dinh Truong Nguyen,‡[b] Trung Hieu Le,[a] Lam Son Le,[a] Nga Hang Thi Phan,[b] Thi-Thao-Van Nguyen,[c] Nguyen Van Tiep,[d] Ekaterina Korneeva,[e] Anh Tuyen Luu,[f] My Uyen Dao,[gh] Minh Tuan Nguyen Dinh *[i] and Chinh Chien Nguyen *[gh]

Electrolytic glucose oxidation has garnered great interest in energy-saving hydrogen generation. However, high charge-transfer resistance and inefficient active centers have been recognized as the primary issues for poor electrochemical performance. In this study, for the first time, we offer a novel defect-rich CeO_x/β-$Ni(OH)_2$ composite nanosheet-decorated Ni foam electrocatalyst (denoted as Ce@NF-GA), synthesized *via* a unique hydrothermal approach under the co-participation of glycerol and acetic acid. The employed characterizations unveil a close CeO_x/β-$Ni(OH)_2$ interfacial contact and numerous surface defects (*e.g.*, oxygen vacancies). Such features significantly result in a significant enhancement in the electrocatalytic glucose oxidation reaction. Indeed, the obtained Ce@NF-GA catalyst demands a low potential of 1.31 V to reach a current density of 10 mA cm^{-2}. Additionally, Ce@NF-GA exhibited a high charge transportation capability and stability for 3 consecutive working cycles, corresponding to an outstanding Faradaic efficiency of ~100% toward hydrogen production. The exploration of such novel material discloses a potential pathway for the utilization of Ce-based electrocatalysts for the energy-saving hydrogen production-coupled glucose oxidation reaction.

Received 29th October 2024
Accepted 15th December 2024

DOI: 10.1039/d4na00892h

rsc.li/nanoscale-advances

Open Access Article. Published on 16 December 2024. Downloaded on 6/22/2026 6:06:40 AM.
This article is licensed under a Creative Commons Attribution-NonCommercial 3.0 Unported Licence.

Introduction

Hydrogen fuel has been recognized as the most essential energy carrier on the road toward a sustainable energy system.[1–3] In this context, alkaline electrocatalytic hydrogen generation involving the cathodic hydrogen reaction (HER) and anodic oxygen evolution reaction (OER) has provided a viable platform for industrial scale production. However, the sluggish kinetics of OER-induced high overpotential has been perceived as the critical obstacle causing enormous energy consumption.[4,5]

To address this issue, hybrid water electrolysis has been established as a promising strategy in which anodic processes could be driven by organic oxidation reactions.[6–11] Such an approach offers two features as follows: (i) a significant decrease in energy consumption and (ii) the generation of value-added products.[12,13] Among these, the hydrogen production-coupled glucose oxidation reaction (GOR) has garnered increasing attention over the past few years.[14–16] Glucose is an outstanding candidate for electrochemical reactions owing to its favorable oxidation thermodynamics. Thus, the glucose oxidation reaction possesses a considerably low potential in comparison to OER counterparts. For example, the conversion of glucose to gluconic acid occurs at a potential of 0.05 V *vs.* RHE, which is significantly lower than that of water oxidation (1.23 V).[17–19] Thus, a hydrogen production-coupled GOR offers two essential features: (i) it remarkably reduces the overall working potential in comparison to that of the conventional water splitting and (ii)

[a]*Hue University of Sciences, Hue University, Hue City 530000, Vietnam*
[b]*School of Medicine and Pharmacy, The University of Danang, Danang 550000, Vietnam*
[c]*Graduate University of Science and Technology, Vietnam Academy of Science and Technology, Hanoi 100000, Vietnam*
[d]*Institute of Physics, Vietnam Academy of Science and Technology, 10 Dao Tan, Ba Dinh, Hanoi 10000, Vietnam*
[e]*Flerov Laboratory of Nulear Reactions, Joint Insititute for Nuclear Research, Moscow Reg., Dubna 141980, Russia*
[f]*Center for Nuclear Technologies, Vietnam Atomic Energy Institute, Ho Chi Minh City, 700000, Vietnam*
[g]*Center for Advanced Chemistry, Institute of Research and Development, Duy Tan University, Danang, 550000, Vietnam. E-mail: nguyenchinhchien@duytan.edu.vn*
[h]*Faculty of Natural Sciences, Duy Tan University, Danang, 550000, Vietnam*
[i]*Faculty of Chemical Engineering, University of Science and Technology, The University of Danang, 54 Nguyen Luong Bang, Danang 550000, Vietnam. E-mail: ndmtuan@dut.udn.vn*

† Electronic supplementary information (ESI) available. See DOI: https://doi.org/10.1039/d4na00892h

‡ These authors contributed equally.

© 2025 The Author(s). Published by the Royal Society of Chemistry

Open Access Article. Published on 16 December 2024. Downloaded on 6/22/2026 6:06:40 AM. This article is licensed under a Creative Commons Attribution-NonCommercial 3.0 Unported Licence.

generates value-added chemical products (*e.g.*, glucaric acid and gluconic acid).[20–22] Nevertheless, the performance of electrocatalytic glucose oxidation has been suffering from low activity owing to the multi-electron transfer process and poor glucose-catalytic surface interaction.[23]

Noble metals (*e.g.*, Au and Pt) have shown strong capabilities toward the GOR. However, their high cost poses challenges for further development.[24] Recently, non-precious metals have made notable progress in enhancing electrocatalytic performance. Among these, CeO_2-based electrocatalysts have emerged as potential candidates for electrochemical oxidation reactions because of the following two features: (i) low-cost materials in comparison to other rare metal/metal oxides; (ii) CeO_2 containing numerous structural defects (*e.g.*, oxygen vacancies) provides an excellent scaffold for the adsorption and oxidation of various substances.[25] Indeed, CeO_2-containing oxygen vacancies are considered the primary factor for lowering energy barriers and accelerating oxidation processes.[26,27]

However, high charge resistance and poor surface properties (*e.g.*, oxygen vacancies) could be considered as the primary reasons, restricting the oxidation properties of the bare CeO_2-based electrocatalysts. Therefore, anchoring CeO_2 active centers onto appropriate support (*e.g.*, β-$Ni(OH)_2$ nanosheet-based materials) could be considered a viable tactic, which not only enhances charge transfer but also efficiently harvests catalytic oxidation capabilities of CeO_2.

The presented investigation attempts to offer a novel defect-rich CeO_x/β-$Ni(OH)_2$ nanosheets composite-decorated nickel foam for the first time. Indeed, three essential aspects have been explored as follows: (i) the preparation of CeO_x/β-$Ni(OH)_2$ composite nanosheets could be obtained under the facile hydrothermal synthesis, in which the co-existence of glycerol and acetic acid significantly drives the formation of the nanosheet architecture; (ii) an intimate interfacial contact between CeO_x and β-$Ni(OH)_2$ nanosheets significantly promotes the charge transportation; and (iii) rich oxygen vacancies offer an appropriate medium for the chemical conversion. Such outcomes result in an outstanding enhancement in the electrocatalytic performance of the prepared CeO_x/β-$Ni(OH)_2$ composite nanosheets-decorated NF electrode towards the energy-saving hydrogen production *via* electrocatalytic oxidation of glucose.

Experimental

Chemicals

Cerium nitrate hexahydrate ($Ce(NO_3)_3 \cdot 6H_2O$, 98%), glycerol ($C_3H_5(OH)_3$, 99%), and acetic acid (CH_3COOH, 99%) were purchased from Sigma-Aldrich. Nickel foam (NF) (99.9%) was supplied by Beijing Beike 2D Materials Co., Ltd. All reagents were used as received without further purification.

Synthesis of Ce-based electrocatalyst

Prior to use, a 3 cm × 3 cm piece of nickel foam (NF) was soaked in 1 M HCl for 45 minutes, sonicated in 96% ethanol for 20 minutes, and then dried at 60 °C for 3 hours. For the synthesis of Ce@NF-GA, 0.2 g of $Ce(NO_3)_3 \cdot 6H_2O$, 2 g of glycerol and 0.95 mL of acetic acid were dissolved in 40 mL of distilled water under continuous stirring for 2 hours. The resulting solution was then transferred to a 100 mL Teflon-lined stainless steel autoclave, containing the treated NF. The autoclave was subjected to hydrothermal treatment at 160 °C for 16 hours. After the reaction, the obtained Ce@NF-GA product was thoroughly washed with distilled water and ethanol, followed by drying at 60 °C for 24 hours. For comparison purposes, the Ce@NF, Ce@NF-G and Ce@NF-A catalysts were synthesized using the same hydrothermal method but without glycerol and/or acetic acid.

Characterization

The morphologies and microstructures of the as-prepared catalysts before and after stability testing were characterized by scanning electron microscopy (SEM, Tescan Vega) and transmission electron microscopy (HR-TEM, Talos Fi200). The crystallographic structure of the samples was examined by powder X-ray diffraction (XRD, Smartlab, Rigaku). The Raman spectra of the obtained samples were recorded on a LabRAM Horiba spectrometer. X-ray photoelectron spectroscopy (XPS) measurements were performed on a Thermo Fisher Scientific instrument.

Electrochemical measurements

To study the electrocatalytic properties of the obtained electrocatalysts, a three-electrode system was employed for all electrochemical tests, where the as-synthesized sample, Hg/HgO electrode, and platinum sheet served as the working electrode, reference electrode, and counter electrode, respectively. The catalytic activity of the samples was measured using a CS310M EIS potentiostat/galvanostat with 1.0 M KOH and 0.1 M glucose solution as the electrolyte. Prior to testing, cyclic voltammetry (CV) cycles were performed at a scan rate of 10 mV s^{-1} to activate the working electrodes. The polarization curves were recorded using the linear sweeping voltammetry (LSV) with the scan rate of 5 mV s^{-1}. The electrochemical impedance spectroscopy (EIS) was carried out at a potential of 0.3 V with an amplitude of 5 mV in the frequency range from 10 kHz to 0.1 Hz in 1.0 M KOH and 0.1 M glucose electrolyte. The electrochemically active surface area (ECSA) was determined based on the double-layer capacitance (C_{dl}) value, which was assessed using CV curves under various scan rates (10–100 mV s^{-1}). The cell voltage test was performed using a two-electrode setup, with NF and Ce@NF-GA electrodes serving as the counter and working electrodes, respectively, at a scan rate of 5 mV s^{-1}. The stability of catalysts was evaluated by a chronoamperometry test at a constant potential of 1.30 V *vs.* RHE for 9 hours. The potential values *versus* Hg/HgO were converted to the values *versus* RHE according to the following equation.[28,29]

$$E_{RHE} = E_{vs.\ Hg/HgO} + 0.059 \times pH + E^{0}_{Hg/HgO} \quad (1)$$

Faradaic efficiency (FE) was determined from the following equation.

Open Access Article. Published on 16 December 2024. Downloaded on 6/22/2026 6:06:40 AM. This article is licensed under a Creative Commons Attribution-NonCommercial 3.0 Unported Licence.

$$\mathrm{FE} = \frac{n \times F \times m_{\mathrm{product}}}{Q} \times 100\% \quad (2)$$

where n number of required electrons for the reaction ($n = 2$); m is the mole of H_2 measured by the water displacement method; F is the Faradaic constant, and Q is the total charge calculated from chronoamperometry measurements.

Results and discussion

The synthesis of the defect-rich CeO_x/β-$Ni(OH)_2$/NF electrode was conducted *via* a one-step hydrothermal treatment, involving the participation of nickel foam (NF), Ce^{4+} cations, glycerol and acetic acid at 160 °C for 16 hours, as shown in Scheme 1 (see section Experimental for the details). It is noteworthy that the presence of glycerol and acetic acid molecules induces a synergistic effect, driving the formation of defect-rich CeO_x/β-$Ni(OH)_2$ nanosheets onto the NF scaffold. Such preparation has been explored for the first time.

Fig. 1 depicts the scanning electron microscopy (SEM) images of the as-prepared CeO_x/β-$Ni(OH)_2$/NF composite (denoted as Ce@NF-GA). In this context, SEM characterization was performed for comparison of samples prepared without acid or/and glycerol (denoted as Ce@NF-G, Ce@NF-A, Ce@NF and bare-NF), as shown in Fig. S1–4.† A smooth surface of the bare NF sample could be observed. Ce@NF-G and Ce@NF samples revealed the existence of tiny particles, whereas Ce@NF-A displays a similar surface as the bare NF sample, suggesting the limited deposition of the synthesized species. In contrast, the Ce@NF-GA material exhibits a distinct morphology, which involves the formation of nanosheets, as shown in Fig. 1A–C. Furthermore, Fig. 1D–H exhibits the EDX spectra and elemental mapping of the Ce@NF-GA sample in which the Ce, Ni and O elements can be found. Moreover, Ce atoms account for ~2%, suggesting uniform distribution of Ce species onto the nanosheet scaffold.

Next, the X-ray diffraction (XRD) characterization was employed to investigate the crystallinity of the prepared samples, as shown in Fig. 2A and B. All samples show two characteristic peaks at 44.5° and 51.8° corresponding to (111) and (200) facets of Ni metal (JCPDS No. 65-2865), respectively (Fig. 2A). The Ce@NF sample exhibits the diffraction peaks centered at two theta of 28.6°, 33.1°, 47.4°, 56.3°, 59.1°, which could be indexed to the (111), (200), (220), (311) and (222) facets, respectively, of the CeO_2 cubic phase (JCPDS No. 81-9325).[30–33]

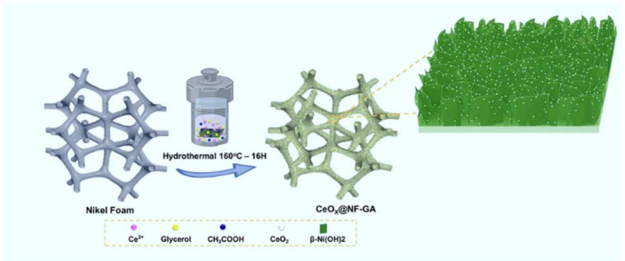

Scheme 1 Schematic of the synthesis of the Ce@NF-GA sample.

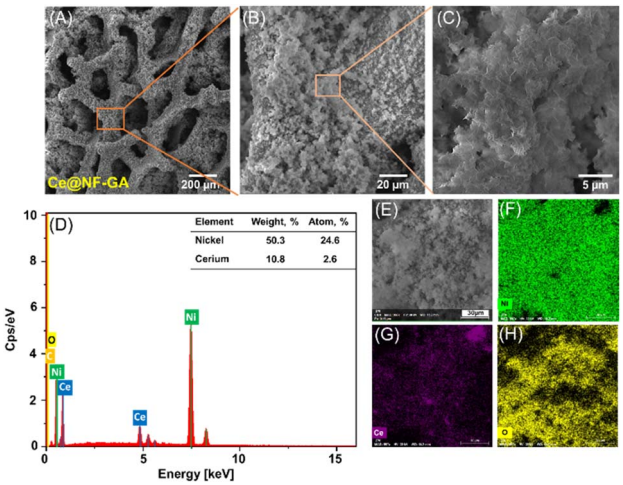

Fig. 1 SEM images (A–C), EDX spectra (D) and elemental mapping (E–H) of the as-prepared Ce@NF-GA sample.

The XRD pattern of the Ce@NF-A sample reveals the characteristic peaks located at 19.1°, 33.1°, 38.4° and 59.3°, corresponding to the β-$Ni(OH)_2$ phase (JCPDS No. 14-0117), whereas the Ce@NF-G sample reveals peaks at 28.6°, 33.1°, 47.4°, 56.3°,

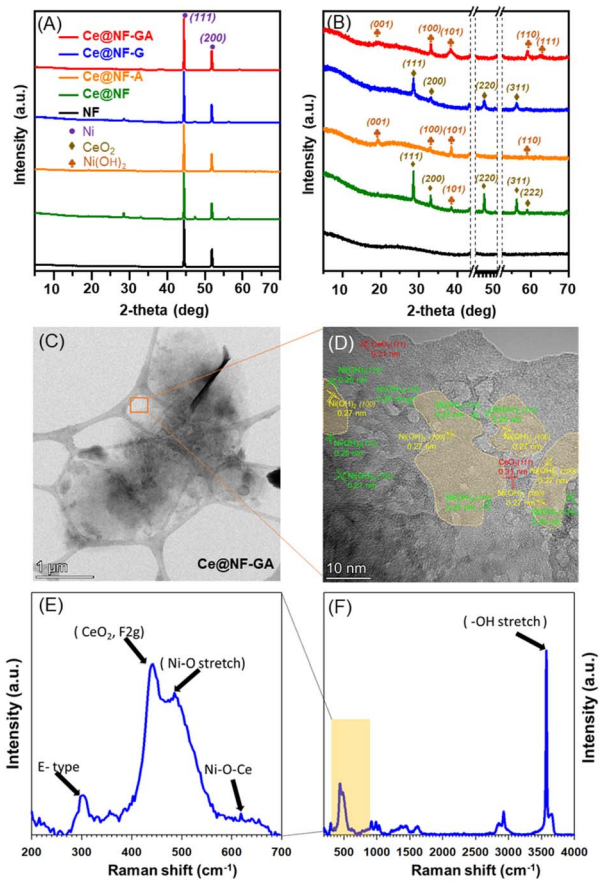

Fig. 2 XRD patterns (A), corresponding magnification of XRD patterns (B) of the as-prepared samples, TEM and HR-TEM image (C and D) and Raman spectra (E and F) of Ce@NF-GA.

© 2025 The Author(s). Published by the Royal Society of Chemistry

Open Access Article. Published on 16 December 2024. Downloaded on 6/22/2026 6:06:40 AM. This article is licensed under a Creative Commons Attribution-NonCommercial 3.0 Unported Licence.

which could be assigned to the CeO_2 phase.[34–37] The XRD pattern of the Ce@NF-GA sample shows characteristic signals, which can be indexed to β-$Ni(OH)_2$ (JCPDS No. 14-0117).[38–40] Moreover, the XRD signals associated with the CeO_2 phase are absent, which could be due to low loading and small particles of CeO_2.

Fig. 2C, D and S5† exhibit the high-resolution transmission electron microscopy (HR-TEM) analysis of the prepared materials. As shown in Fig. S5,† the lattice spacing values of 0.20, 0.27 and 0.31 nm corresponding to (220), (200) and (111) planes of CeO_2, respectively, are observed in Ce@NF and Ce@NF-G samples.[41–43] Additionally, an interplanar spacing of 0.25 nm, attributed to the (001) plane of $Ni(OH)_2$ phase, is also recognized.[44] The TEM and HR-TEM images of the Ce@NF-GA sample unambiguously exhibit the nanosheet structure, as shown in Fig. 2C and D. The lattice spacing values of 0.25 nm and 0.27 nm can be attributed to the (110) and (100) planes, respectively, of the β-$Ni(OH)_2$ nanosheets.[45–47]

Fig. 2E, F and S6† exhibit the Raman spectra of the prepared catalysts. It can be seen that the Ce@NF-G and Ce@NF samples exhibit three distinct regions as follows: (i) a characteristic peak centered at 450 cm^{-1} could be assigned to the F 2g vibration mode of the cubic-fluorite CeO_2 structure (Fig. S6†); (ii) D bands centered in the region of ~500–700 cm^{-1} could be assigned to the oxygen vacancies (Fig. S6†) and (iii) 2LO bands is located in the region of 900–1200 cm^{-1}. [48,49] The Raman spectrum of Ce@NF-GA shows a weak and redshift of the F 2g Raman peak to 440 cm^{-1} (Fig. 2E), suggesting the formation of small CeO_2 particles and the Ni species–CeO_2 interaction.[50–52] This Ce@NF-GA sample also exhibits a high peak ratio of D/F 2g bands implying rich oxygen vacancies-containing CeO_2.[51,52] Moreover, notable peaks centered at 296, 486 and 3574 cm^{-1} could be attributed to E-type vibration of Ni–OH lattice, Ni–O stretching and symmetric stretching mode of –OH of β-$Ni(OH)_2$, respectively.[45,53] Interestingly, a peak arising at 619 cm^{-1} could be assigned to the Ni–O–Ce bond.[54,55]

X-ray photoelectron spectroscopy (XPS) was employed to analyze the oxidation states of O, Ni and Ce elements in the prepared materials. The survey spectrum reveals strong peaks corresponding to Ce 3d, Ni 2p, O 1s and C 1s elements, which are in good agreement with EDX studies (Fig. S7†). The adventitious carbon centered at 284.8 eV was used for the calibration, as shown in Fig. 3A. Fig. 3B shows the Ce $3d_{3/2}$ deconvolution of the Ce@NF-GA sample. The peak centered at 903.2 eV is attributed to the Ce^{3+} oxidation state, while four primary peaks centered at 898.2, 900.7, 907.1 and 916.5 eV, could be assigned to Ce^{4+}.[56–58] The Ce^{3+}/Ce^{4+} peak area ratio is found to be significantly higher than those of compared Ce@NF and Ce@NF-G samples (Table S1†). In other words, the presence of high Ce^{3+} concentration originated from the presence of numerous oxygen vacancies in the Ce@NF-GA electrocatalyst.[59,60] The Ni 2p XPS spectra of Ce@NF-GA can be separated into three components, as shown in Fig. 3C. The peak located at a binding energy of 853.2 eV corresponds to metallic Ni.[61] Additional peaks positioned at ~855.5 and 857.1 eV are associated with Ni^{2+} and Ni^{3+} states, respectively.[62,63] These peaks shift to lower binding energy in comparison to the bare

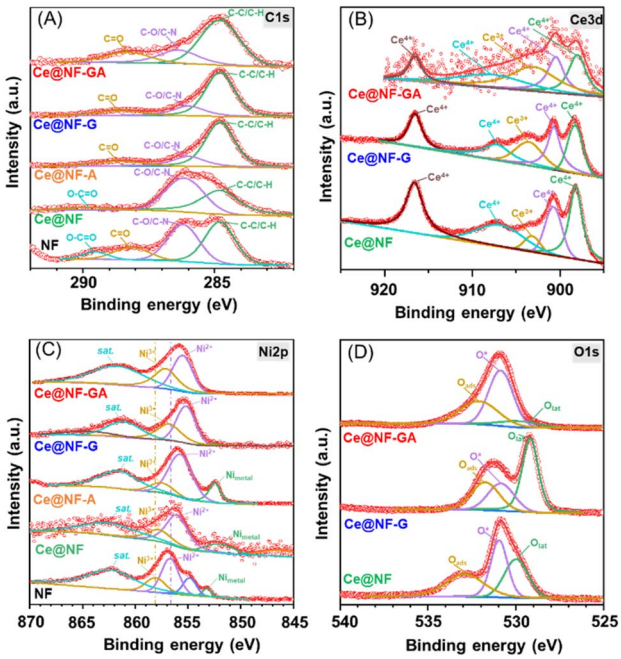

Fig. 3 XPS spectra of C 1s (A), Ce 3d (B), Ni 2p (C), and O 1s (D) of the as-prepared samples.

NF sample, suggesting the strong interaction between the formed CeO_2 and β-$Ni(OH)_2$, possibly due to charge transfer effects or chemical bonding. The O 1s spectra of the Ce@NF-GA sample (Fig. 3D) could be deconvoluted into three distinct peaks centered at 529.8, 530.8 and 532.6 eV, which could be assigned to lattice oxygen, low coordination oxygen species and adsorbed H_2O molecules, respectively.[64,65] Impressively, the area percentage of surface oxygen was 35.4%, which is significantly higher than those of compared Ce@NF (17.4%) and Ce@NF-G (22.7%) samples. The mentioned findings suggest a high concentration of surface oxygen (*e.g.*, oxygen vacancies, hydroxyl groups) in the Ce@NF-GA sample, which could enhance the electrochemical performance.[66] To this end, the investigated characterizations of the Ce@NF-GA sample unveil three essential points: (i) the formation of nanosheet CeO_x/β-$Ni(OH)_2$ architecture resulting through a unique synthetic method; (ii) the existence of the CeO_x/β-$Ni(OH)_2$ intimate contact *via* a direct chemical bonding, which can facilitate the charge transportation and (iii) the CeO_x/β-$Ni(OH)_2$ nanosheets containing a numerous number of oxygen vacancies could provide a robust platform for electrochemical processes.

The next attempt was aimed at evaluating the electrochemical performance of the prepared catalysts for the glucose oxidation reaction (GOR). The electrochemical tests were conducted in a standard three-electrode reactor, using the synthesized samples, Hg/HgO and Pt as the working, reference and counter electrodes, respectively. Fig. S8† illustrates the linear sweep voltammetry (LSV) curves of Ce@NF-GA in 1.0 M KOH solution with and without 0.10 M glucose. It can be seen that the Ce@NF-GA electrode significantly promotes the glucose oxidation reaction; the potential required for this sample to

Open Access Article. Published on 16 December 2024. Downloaded on 6/22/2026 6:06:40 AM.
This article is licensed under a Creative Commons Attribution-NonCommercial 3.0 Unported Licence.

achieve a similar current density is considerably lower than that of the oxygen evolution reaction (OER) counterpart. This suggests a potential alternative tactic for energy-saving hydrogen production. The LSV results of the as-prepared materials are presented in Fig. 4A. The Ce@NF-GA sample requires a low potential of 1.31 V *vs.* RHE to reach the current density of 10 mA cm^{-2}, which is significantly lower than those of Ce@NF (1.41 V *vs.* RHE) and bare-NF (1.44 V *vs.* RHE). The obtained results, compared to previous studies, as shown in Table S2,† indicate outstanding catalytic activity of the prepared Ce@NF-GA electrocatalyst.

To investigate the kinetics of glucose electrooxidation, the Tafel plot was derived from the LSV curve at a low scan rate of 0.1 mV s^{-1}. As shown in Fig. S9† the Tafel slope of Ce@NF-GA (157 mV dec^{-1}) is significantly lower than that of the compared samples. In other words, the prepared Ce@NF-GA catalyst significantly promotes the conversion of glucose. The electrochemical active surface area (ECSA) of the samples was evaluated *via* CV measurements in the non-faradaic region (*c.a.*, 0.50–0.60 V *vs.* RHE), as depicted in Fig. S10.† The Ce@NF-GA possesses the largest C_{dl} of 2.4 mF cm^{-2}, which is significantly higher than those of Ce@NF (*c.a.*, 1.1 mF cm^{-2}), Ce@NF-G (*c.a.*, 0.8 mF cm^{-2}), Ce@NF-A (*c.a.*, 0.2 mF cm^{-2}) and bare-NF (*c.a.*, 0.2 mF cm^{-2}) samples. Furthermore, electrochemical impedance spectroscopy (EIS) was conducted to investigate the charge transfer of the prepared catalysts, as shown in Fig. 4B. The Ce@NF-G displays the smallest charge-transfer resistance compared to the rest of the samples, suggesting a high charge-transfer capability of the Ce@NF-GA material. Undoubtedly, rich defects CeO_2/β-$Ni(OH)_2$ nanosheet architecture-containing Ce@NF-GA catalysts could be considered the primary driver for such outstanding activity performance.

To this end, the obtained CeO_x/β-$Ni(OH)_2$ nanosheets configuration bears two essential features as follows: (i) numerous CeO_x catalytic sites to drive the catalytic steps of the glucose oxidation and (ii) the intimate contact in CeO_x-β-$Ni(OH)_2$ significantly promotes the charge migration. In this situation, such contact could build in an interfacial charge polarization, [67,68] encouraging electron flows from glucose to the counter electrode.

Stability is one of the important factors in evaluating the applicability of electrocatalysts in large-scale use. The chronopotentiometry measurement was conducted as exhibited in Fig. 4C. Notably, Ce@NF-GA displays stability with a decrease in current density after 3 consecutive cycles (*c.a.*, 9 working hours). Additionally, the amount of the produced hydrogen was also measured. The Ce@NF-GA produces the hydrogen evolution rates of 0.15 and 0.8 mmol cm^{-2} h^{-1} at 1.30 V and 1.56 V *vs.* RHE, respectively, corresponding to the Faradaic efficiencies of ~100%. Moreover, a Ce@NF-GA‖NF cell requires a voltage of 1.61 V to reach the current density of 10 mA cm^{-2} for the GOR application, which is considerably lower than that of the OER counterpart (1.85 V), as shown in Fig. 4D. These results suggest that Ce@NF-GA exhibits outstanding catalytic efficiency, making it a promising candidate for electrochemical applications.

Besides, SEM and XRD characteristics of the Ce@NF-GA sample after a total of 9 working hours were investigated. As shown in Fig. S11,† the morphology and elemental composition remained virtually unchanged. Moreover, Fig. S12† exhibits the XRD patterns of the Ce@NF-GA sample before and after the stability test. Notably, a peak centering at two theta of 28.5° appears in the post-catalytic sample, which could be attributed to the CeO_2 (111) facet. This piece of evidence suggests the agglomeration of CeO_2 particles, which is believed as the primary reason for the decrease in current.

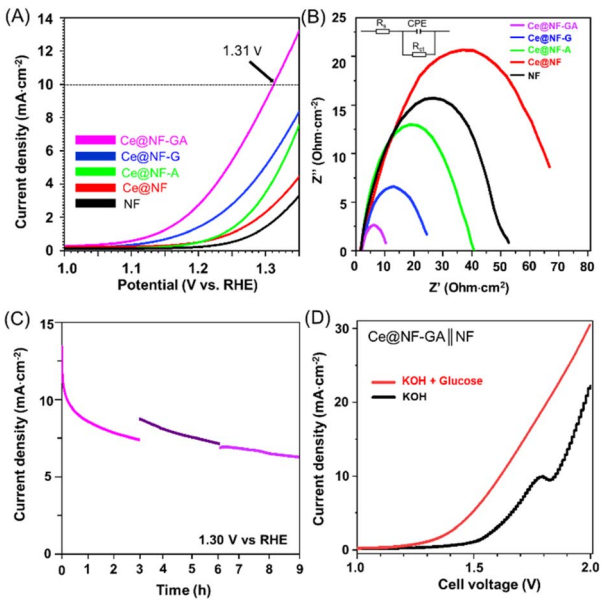

Fig. 4 LSV curves (A), Nyquist plots (the inset: a fitted equivalent circuit consisting of R_s, CPE, and R_{ct}) (B) of the as-prepared samples and chronopotentiometry curves of Ce@NF-GA (C) and cell voltage comparison of glucose electrolysis and water electrolysis with Ce@NF-GA (D) at a scan rate of 5 mV s^{-1}.

Conclusions

In summary, a unique and defects-rich CeO_x/$Ni(OH)_2$ nanosheets composite-decorated nickel foams were synthesized for the first time. The co-existence of glycerol and acetic acid is the paramount factor, driving the formation of the nanosheet structure. The obtained material possessing an intimate interfacial CeO_x-β-$Ni(OH)_2$ contact, a high concentration of oxygen vacancies offers an outstanding scaffold for the electrocatalytic oxidation of glucose. Indeed, the Ce@NF-GA sample required a low potential of 1.31 V *vs.* RHE to reach a current density of 10 mA cm^{-2}. Such achievements could be rooted in the large electrochemical active surface and low charge transfer resistance within the Ce@NF-GA electrocatalysts. Moreover, the investigation of chronoamperometry illustrates the stability of Ce@NF-GA with a slight decrease in the current density for 9 h, corresponding to the FE of ~100%. This study offers a novel strategy for developing a catalyst for energy-saving hydrogen production *via* electrocatalytic glucose oxidation.

© 2025 The Author(s). Published by the Royal Society of Chemistry

Open Access Article. Published on 16 December 2024. Downloaded on 6/22/2026 6:06:40 AM. This article is licensed under a Creative Commons Attribution-NonCommercial 3.0 Unported Licence.

Data availability

Data are provided within the manuscript and its ESI.†

Author contributions

Cong Hong Nhat Nguyen: methodology, formal analysis, investigation. Dinh Truong Nguyen: data curation, investigation. Trung Hieu Le, Lam Son Le: methodology, validation. Nga Hang Thi Phan: methodology. Thi-Thao-Van Nguyen, Nguyen Van Tiep, Ekaterina Korneeva, Anh Tuyen Luu, My Uyen Dao: methodology, formal analysis, resources. Minh Tuan Nguyen Dinh: supervision, resources, writing – review. Chinh Chien Nguyen: supervision, writing – review, writing – original draft and editing.

Conflicts of interest

There are no conflicts to declare.

Acknowledgements

The authors acknowledge the support of Hue University under the Core Research Group Program, Grant No. NCTB.DHH.2024.09.

References

1 Z.-Y. Yu, Y. Duan, X.-Y. Feng, X. Yu, M.-R. Gao and S.-H. Yu, *Adv. Mater.*, 2021, **33**, 2007100.
2 H. Ding, Z. Zhao, H. Zeng, X. Li, K. Cui, Y. Zhang and X. Chang, *ACS Mater. Lett.*, 2024, **6**, 1029–1041.
3 Y. Wang, M. Zhang, Y. Liu, Z. Zheng, B. Liu, M. Chen, G. Guan and K. Yan, *Adv. Sci.*, 2023, **10**, 2207519.
4 T. Gao, Q. An, X. Tang, Q. Yue, Y. Zhang, B. Li, P. Li and Z. Jin, *Phys. Chem. Chem. Phys.*, 2024, **26**, 19606–19624.
5 J.-Y. Zhang, T. He, M. Wang, R. Qi, Y. Yan, Z. Dong, H. Liu, H. Wang and B. Y. Xia, *Nano Energy*, 2019, **60**, 894–902.
6 X. Liu, P. Cai, G. Wang and Z. Wen, *Int. J. Hydrogen Energy*, 2020, **45**, 32940–32948.
7 X. Han, H. Sheng, C. Yu, T. W. Walker, G. W. Huber, J. Qiu and S. Jin, *ACS Catal.*, 2020, **10**, 6741–6752.
8 K. Yang, L. Hao, Y. Hou, J. Zhang and J.-H. Yang, *Int. J. Hydrogen Energy*, 2024, **51**, 966–981.
9 C. Ding, F. Dong and Z. Tang, *ChemistrySelect*, 2020, **5**, 13318–13340.
10 Y. Qiu, Y. Zhang, M. Yu, X. Li, Y. Wang, Z. Ma and S. Liu, *Small*, 2024, **20**, 2310087.
11 Y. Qiu, X. Dai, Y. Wang, X. Ji, Z. Ma and S. Liu, *J. Colloid Interface Sci.*, 2023, **629**, 297–309.
12 S. Sun, Z. Liu, Z. J. Xu and T. Wu, *Appl. Catal., B*, 2024, **358**, 124404.
13 K. Lu, Y. Zhang, Y. Shen and H. Li, *Catal. Sci. Technol.*, 2024, **14**, 2973–2990.
14 Y. Wang, W. Yan, M. Ni, C. Zhu and H. Du, *Chem. Commun.*, 2023, **59**, 2485–2488.
15 H. Sun, X. Xu, L. Fei, W. Zhou and Z. Shao, *Adv. Energy Mater.*, 2024, **14**, 2401242.
16 Z. Chen, W. Wei, L. Song and B.-J. Ni, *Sustain. Horiz.*, 2022, **1**, 100002.
17 W. S. Fonseca, T. Rafaïdeen, H. Kahri, T. W. Napporn and C. Coutanceau, *Electrochim. Acta*, 2025, **510**, 145367.
18 S. A. Patil, A. C. Khot, K. D. Kadam, H. T. Bui, H. Im and N. K. Shrestha, *Inorg. Chem. Front.*, 2023, **10**, 7204–7211.
19 X. Lin, H. Zhong, W. Hu and J. Du, *Inorg. Chem.*, 2023, **62**, 10513–10521.
20 X. Wu, Z.-J. Zhao, X. Shi, L. Kang, P. Das, S. Wang, S. Chu, H. Wang, K. Davey, B. Zhang, S.-Z. Qiao, J. Gong and Z.-S. Wu, *Energy Environ. Sci.*, 2024, **17**, 3042–3051.
21 D. Mehta, S. Kaur, N. Thakur and T. C. Nagaiah, *J. Mater. Chem. A*, 2023, **11**, 25507–25515.
22 A. Chaturvedi, S. Gaber, S. Kaur, K. C. Ranjeesh, T. C. Nagaiah and D. Shetty, *ACS Energy Lett.*, 2024, **9**, 2484–2491.
23 X. Wu, G. R. Lin, C. Zhang, H. Liao, Y. Qian, X. Sun, Y. Zhang, S. Chen and P. Gao, *Int. J. Hydrogen Energy*, 2024, **86**, 511–518.
24 Y.-L. Men, P. Liu, Y. Liu, X.-Y. Meng and Y.-X. Pan, *Ind. Eng. Chem. Res.*, 2022, **61**, 4300–4309.
25 G. S. de Luna, P. Zeller, E. Öztuna, F. Maluta, A. Canciani, F. Ospitali, P. H. Ho, A. Paglianti, A. Knop-Gericke, G. Fornasari, J. J. Velasco-Vélez and P. Benito, *ACS Catal.*, 2023, **13**, 12737–12745.
26 Y. Li, H. Li, K. Li, R. Wang, R. Zhang and R. Liu, *ACS Appl. Nano Mater.*, 2023, **6**, 14214–14227.
27 X. Yang, L. Sun, X. Liu, Z. Yang, H. Sun, W. Liu and H. Chen, *ACS Catal.*, 2024, **14**, 6236–6246.
28 J. N. Hausmann, B. Traynor, R. J. Myers, M. Driess and P. W. Menezes, *ACS Energy Lett.*, 2021, **6**, 3567–3571.
29 X. Chen, Z. Zhang, Y. Yang, B. Hu, Q. Wu, W. Fan, J. Hao and W. Shi, *Chem. Eng. Sci.*, 2024, **291**, 119937.
30 Y. Huang, B. Long, M. Tang, Z. Rui, M.-S. Balogun, Y. Tong and H. Ji, *Appl. Catal., B*, 2016, **181**, 779–787.
31 J. Hao, Z. Long, L. Sun, W. Zhan, X. Wang and X. Han, *Inorg. Chem.*, 2021, **60**, 7732–7737.
32 X. Zhou, J. Ling, W. Sun and Z. Shen, *J. Mater. Chem. A*, 2017, **5**, 9717–9722.
33 X. Niu and F. Tu, *J. Mater. Sci.: Mater. Electron.*, 2017, **28**, 2141–2146.
34 Z. Wu, X.-L. Huang, Z.-L. Wang, J.-J. Xu, H.-G. Wang and X.-B. Zhang, *Sci. Rep.*, 2014, **4**, 3669.
35 S. A. A. R. Sayyed, N. I. Beedri, V. S. Kadam and H. M. Pathan, *Bull. Mater. Sci.*, 2016, **39**, 1381–1387.
36 C. Wang, F. Yu, M. Zhu, C. Tang, L. Dong and B. Dai, *ACS Omega*, 2018, **3**, 5692–5703.
37 Z. Qin, Y. Wang, X. Huang, W. Shen, J. Yu and J. Li, *J. Inorg. Organomet. Polym. Mater.*, 2020, **30**, 2089–2097.
38 V. Sannasi, K. U. Maheswari, C. Karthikeyan and S. Karuppuchamy, *Ionics*, 2020, **26**, 4067–4079.
39 E. Gobinath, M. Dhatchinamoorthy, P. Saran, D. Vishnu, R. Indumathy and G. Kalaiarasi, *Results Chem.*, 2023, **6**, 101043.

© 2025 The Author(s). Published by the Royal Society of Chemistry

Open Access Article. Published on 16 December 2024. Downloaded on 6/22/2026 6:06:40 AM. This article is licensed under a Creative Commons Attribution-NonCommercial 3.0 Unported Licence.

40 G. Cheng, Q. Bai, C. Si, W. Yang, C. Dong, H. Wang, Y. Gao and Z. Zhang, *RSC Adv.*, 2015, **5**, 15042–15051.
41 P. S. M. Kumar, S. Thiripuranthagan, T. Imai, G. Kumar, A. Pugazhendhi, S. R. Vijayan, R. Esparza, H. Abe and S. K. Krishnan, *ACS Sustain. Chem. Eng.*, 2017, **5**, 11290–11299.
42 Y. Liu, Z. Yang, X. Zhang, Y. He, J. Feng and D. Li, *Catal. Lett.*, 2019, **149**, 361–372.
43 D. Channei, K. Chansaenpak, P. Jannoey and S. Phanichphant, *Solid State Sci.*, 2019, **96**, 105951.
44 J. L. Gunjakar, A. I. Inamdar, B. Hou, S. Cha, S. M. Pawar, A. A. Abu Talha, H. S. Chavan, J. Kim, S. Cho, S. Lee, Y. Jo, H. Kim and H. Im, *Nanoscale*, 2018, **10**, 8953–8961.
45 W. Yang, M. Peng, Y. Lv, M. Sun, J. Zhang, W. Li and Y. Fu, *Chem. Eng. J.*, 2023, **475**, 146138.
46 Q. Cao, M. Luo, Y. Huang, Q. Liu, X. Kong, J. Lei, Z. Jiang and J. Wang, *Sustainable Energy Fuels*, 2020, **4**, 1522–1531.
47 X. Yi, V. Celorrio, H. Zhang, N. Robertson and C. Kirk, *J. Mater. Chem. A*, 2023, **11**, 22275–22287.
48 N. A. Rahman, K. T. Wong, C. E. Choong, I. W. Nah, C. M. Park, J. R. Kim, S.-E. Oh, Y. Yoon, E. H. Choi and M. Jang, *Appl. Surf. Sci.*, 2025, **679**, 161174.
49 L. Xue, C. Zhang, J. Wu, Q.-Y. Fan, Y. Liu, Y. Wu, J. Li, H. Zhang, F. Liu and S. Zeng, *Appl. Catal., B*, 2022, **304**, 120951.
50 S. Loridant, *Catal. Today*, 2021, **373**, 98–111.
51 S. Mahammadunnisa, P. M. K. Reddy, N. Lingaiah and C. Subrahmanyam, *Catal. Sci. Technol.*, 2013, **3**, 730–736.
52 F. Yang, X. Bao, P. Li, X. Wang, G. Cheng, S. Chen and W. Luo, *Angew. Chem., Int. Ed.*, 2019, **58**, 14179–14183.
53 G. Liu, Y. Qin, Y. Lyu, M. Chen, P. Qi, Y. Lu, Z. Sheng and Y. Tang, *Chem. Eng. J.*, 2021, **426**, 131248.
54 Y. Huang, X. Pang, J. Cui, Z. Huang, G. Wang, H. Zhao, H. Bai and W. Fan, *Inorg. Chem.*, 2023, **62**, 6499–6509.
55 S. F. Zai, X. Y. Gao, C. C. Yang and Q. Jiang, *Adv. Energy Mater.*, 2021, **11**, 2101266.
56 J. Lian, P. Liu, C. Jin, Z. Shi, X. Luo and Q. Liu, *Microchim. Acta*, 2019, **186**, 332.
57 Y.-L. Zheng, D.-S. Mao, S.-S. Sun and G.-Y. Fu, *J. Mater. Sci.*, 2016, **51**, 917–925.
58 T. Hu, J. Liu, H. Yuan, L. Zhang and Y. Wang, *ChemSusChem*, 2024, **17**, e202301078.
59 D. Pal, D. Maity, A. Sarkar, D. Sarkar and G. G. Khan, *J. Colloid Interface Sci.*, 2022, **620**, 209–220.
60 T. Xia, S. Yao, Z. Wu, G. Li and J. Li, *J. Hazard. Mater.*, 2022, **424**, 127700.
61 Z. Lv, X. Tan, C. Wang, A. Alsaedi, T. Hayat and C. Chen, *Chem. Eng. J.*, 2020, **389**, 123428.
62 N. Chen, S. Che, H. Liu, N. Ta, G. Li, F. Chen, G. Ma, F. Yang and Y. Li, *Catalysts*, 2022, **12**, 1319.
63 M. A. Peck and M. A. Langell, *Chem. Mater.*, 2012, **24**, 4483–4490.
64 K. Nie, Y. Yuan, X. Qu, B. Li, Y. Zhang, L. Yi, X. Chen and Z. Liu, *J. Colloid Interface Sci.*, 2024, **656**, 168–176.
65 B. Jin, K. Wang, H. Yu, X. He and X. Liang, *Chem. Eng. J.*, 2023, **459**, 141611.
66 Y. Liu, C. Ma, Q. Zhang, W. Wang, P. Pan, L. Gu, D. Xu, J. Bao and Z. Dai, *Adv. Mater.*, 2019, **31**, 1900062.
67 Y. Zhang, Y. Lin, T. Duan and L. Song, *Mater. Today*, 2021, **48**, 115–134.
68 J. Liu, X. Yang, F. Si, B. Zhao, X. Xi, L. Wang, J. Zhang, X.-Z. Fu and J.-L. Luo, *Nano Energy*, 2022, **103**, 107753.

© 2025 The Author(s). Published by the Royal Society of Chemistry